energies

MDPI

Article

Design and Experimental Verification of Hubless Rim-Driven Propulsor Consisting of Bearingless Propeller for an Unmanned Underwater Drone

Myoung-Su Kim [1] and Sung-An Kim [2,*]

[1] Sansystech, Busan 46918, Republic of Korea; mskim@sansystech.co.kr
[2] Electric Power Machinery Team, Electric Propulsion Safety Technology Center, Ulsan Headquarters, Korea Marine Equipment Research Institute, Ulsan 44776, Republic of Korea
* Correspondence: sakim@komeri.re.kr

Abstract: This paper presents the design and experimental verification of a hubless rim-driven propulsor (HRDP) for an unmanned underwater drone. The bearings of the HRDP are required to rotate and fix the propeller. However, the bearing increases the weight and size of the propulsor. Therefore, this paper proposes a structure in which the rotor of a surface-mounted permanent magnet synchronous motor (SPMSM) and a hubless propeller are combined without the bearings in the rim-driven propulsor. The design procedure of the propulsor is established and the response surface method (RSM) is used to design and optimize the proposed structure. The validity of the HRDP with the proposed structure is verified through simulation results using an electromagnetic field (EF) analysis and computational fluid analysis, and test results using a water tank. Finally, compared to the initial HRDP, the weight of the SPMSM in the optimized HRDP is decreased by 7.3%, and by reducing the required torque by about 19%, power consumption is reduced by about 24.66 W.

Keywords: hubless rim-driven propulsor; surface-mounted permanent magnet synchronous motor; response surface method; electromagnetic field analysis; computational fluid analysis

Citation: Kim, M.-S.; Kim, S.-A. Design and Experimental Verification of Hubless Rim-Driven Propulsor Consisting of Bearingless Propeller for an Unmanned Underwater Drone. *Energies* **2023**, *16*, 7458. https://doi.org/10.3390/en16217458

Academic Editor: Chunhua Liu

Received: 17 October 2023
Revised: 1 November 2023
Accepted: 2 November 2023
Published: 6 November 2023

1. Introduction

As the global demand for achieving net zero emissions rapidly increases, there is a growing interest in the development of environmentally friendly means of transportation powered by sustainable energy sources. This surge in interest is not only driven by the urgent need to address climate change but is also spurred by the heightened awareness of the detrimental effects of air pollution, including various types of particulate matter, on the deterioration of air quality [1–4]. This dual concern for reducing greenhouse gas emissions and mitigating air pollution has led to a significant shift in the transportation sector towards cleaner and more sustainable mobility solutions.

Ocean transport plays a significant role in global commerce, but it also contributes approximately 3% of the world's total greenhouse gas and pollutant emissions. To put this in perspective, the carbon dioxide (CO_2) emissions generated by a single large ship are equivalent to those produced by 70,000 cars. These alarming statistics have raised growing concerns about the continued reliance on fossil fuels in maritime transportation activities.

The urgency to address environmental and climate challenges has led to a shift away from fossil fuel-based propulsion systems toward the exploration of various hybrid and all-electric propulsion concepts. As international maritime trade continues to grow, the demand for vessel capacity and propulsion power also experiences an annual increase. However, traditional ship propulsion systems face several challenges in meeting these demands.

The complexities associated with structural design, higher construction costs, and reduced ship space utilization pose significant hurdles in adopting more sustainable and efficient propulsion technologies [5–7]. As the maritime industry strives to strike a balance between economic growth and environmental sustainability, innovative solutions are sought to reduce emissions, improve efficiency, and meet the evolving needs of this vital sector.

A hubless rim-driven propulsor (HRDP) represents a groundbreaking advancement in propulsion technology. This novel integrated motor thruster, commonly referred to as a shaftless propeller, operates on a fundamentally different principle compared to traditional propellers. Rather than being powered by a central shaft, the HRDP derives its propulsive force from a circular rim that is firmly connected to the blade tips [8–12].

This innovative design eliminates the need for a traditional shaft and offers several advantages. By utilizing the circular rim to provide torque to the propeller blades, the HRDP achieves enhanced efficiency and maneuverability. The structural attachment of the rim to the blade tips ensures a direct transfer of rotational energy, resulting in improved propulsion performance. In addition to its technical merits, the HRDP offers practical benefits. The absence of a central shaft simplifies the overall propulsion system, reducing complexity and maintenance requirements. Moreover, the elimination of the shaft creates additional space within the vessel, enabling better space utilization and potential for improved cargo capacity. The HRDP represents a significant departure from conventional propulsion systems, presenting a promising solution for efficient and space-saving propulsion in various maritime applications. The innovative shaftless design of the HRDP, driven by the circular rim, opens up new possibilities for optimizing propulsion performance and addressing the evolving needs of the maritime industry [13–17]. Due to the special structure and numerous advantages of the HRDP, research has been conducted on hydrodynamic performance, vibration and noise, scale effects, cavitation performance, and motor electromagnetic performance [18–30].

The inclusion of bearings is necessary for the rotation and fixation of the propeller in an HRDP [31]. In conventional HRDP designs, a bearing is utilized to facilitate the rotation and fixation of the propeller. However, the presence of the bearing adds weight and increases the size of the propulsor. The use of bearings can pose challenges, particularly for battery-powered underwater robots and unmanned underwater drones. The additional weight introduced by the bearings can significantly impact the operational time and over-all endurance of the system. Therefore, this paper focuses on the design and experimental verification of an HRDP specifically developed for an unmanned underwater drone. The objective is to explore alternative design approaches that reduce reliance on traditional bearings and address the weight-related challenges faced by battery-powered underwater drones.

This study proposes a structure where a propeller is placed inside the inner diameter of the permanent magnet synchronous motor (SPMSM) rotor. The propeller is then secured by applying epoxy to the space between the rotor and the propeller and to the outer diameter of the rotor. The stator is placed inside the duct of the HRDP made from acrylonitrile butadiene styrene plastic (ABS), and it is fixed by injecting epoxy into the space between the duct and the stator.

The proposed design procedure for the structure of the HRDP involves mutual basic designs for the combination of the propeller and electric motor, taking into account their interdependence, and then proceeds with optimization using the response surface method (RSM) [32,33]. In the case of the validity of the basic and optimization designs for the HRDP following the proposed design procedure, the propeller is analyzed using the computational fluid dynamics (CFD) analysis, and the SPMSM is validated through electromagnetic field (FE) analysis. The performance of the HRDP manufactured with the proposed structure is verified by manufacturing a water tank identical to the boundary conditions of the CFD analysis. Additionally, the durability of the proposed HRDP structure is verified by continuously operating it for a total of 733 h using a controller inputting command profiles with various speeds applied.

2. Optimization Design and Analysis of HRDP

2.1. Specifications of HRDP

Table 1 presents the specifications of a 400 W class HRDP. Table 2 summarizes the notation adopted in this paper. To minimize hydrodynamic resistance and the load caused by weight, the diameter (D_H) and stack length (D_{H_stk}) of the HRDP has been set to be equal to 90 mm and 35 mm. At the rated speed (N_{P_rated}) of 3300 rpm, the rated thrust (T_{P_rated}) is 25 N or more, and at the maximum speed (N_{P_max}) of 4200 rpm, the maximum thrust (T_{P_max}) is 40 N or more.

Table 1. Required specifications of the HRDP.

Item	Unit	Value
Diameter of HRDP (D_H)	mm	90
Stack length of HRDP (D_{H_stk})	mm	35
Diameter of propeller (D_P)	mm	52
Rated speed of HRDP (N_{P_rated})	rpm	3300
Rated thrust of HRDP (T_{P_rated})	N	≥25
Maximum speed of HRDP (N_{P_max})	rpm	4200
Maximum thrust of HRDP (T_{P_max})	N	≥40

Table 2. Notation and nomenclature used in this paper.

Symbol	Meaning
HRDP	hubless rim-driven propulsor
SPMSM	surface-mounted permanent magnet synchronous motor
RSM	response surface method
EF	electromagnetic field
ABS	acrylonitrile butadiene styrene plastic
P	pitch of propeller
c	chord length of propeller
f	camber of propeller
P/D_P	pitch diameter ratio
f$/c$	chord length ratio
c/D_P	camber ratio
r	radial distance from the center hub of the propeller
R	total radius of the propeller
r_R	non-dimensional radius ratio
α, β	coefficients used to vary non-dimensional radius ratio
T_{P_rated}	rated thrust of HRDP
Q_{P_rated}	required torque of HRDP
TTR	torque-thrust ratio
Q_P	required torque of the propeller
T_P	thrust of the propeller
N_P	speed of the propeller
PRR	reduction ratio
$P_{initial}$	mechanical output power of the initial propeller
$P_{optimized}$	mechanical output power of the optimized propeller
F_F	winding fill factor of SPMSM
η_M	efficiency of SPMSM
T_{M_ripple}	torque ripple of SPMSM
T_{M_rated}	output torque of SPMSM
TRV	torque per unit of the rotor volume
k_{w1}	fundamental harmonic winding factor
A	electric loading
B	magnetic loading
m	number of phases
T_{ph}	number of turns in series per phase
I	RMS phase current

Table 2. *Cont.*

Symbol	Meaning
D	diameter of the airgap
ϕ_1	flux density
p	number of pole pair
L_{stk}	stack length
TW	tooth width
SO	slot opening
MA	magnet arc

2.2. Design and Analysis of Hubless Propeller

Figure 1 represents a flowchart for the design and analysis of the HRDP. Based on the determined parameters D_H, D_{H_stk}, D_P, N_{P_rated}, and T_{P_rated} of the HRDP, the basic design of the propeller with the duct is performed by applying NACA66 airfoils and subsequently evaluating the initial performance of the HRDP through the CFD analysis.

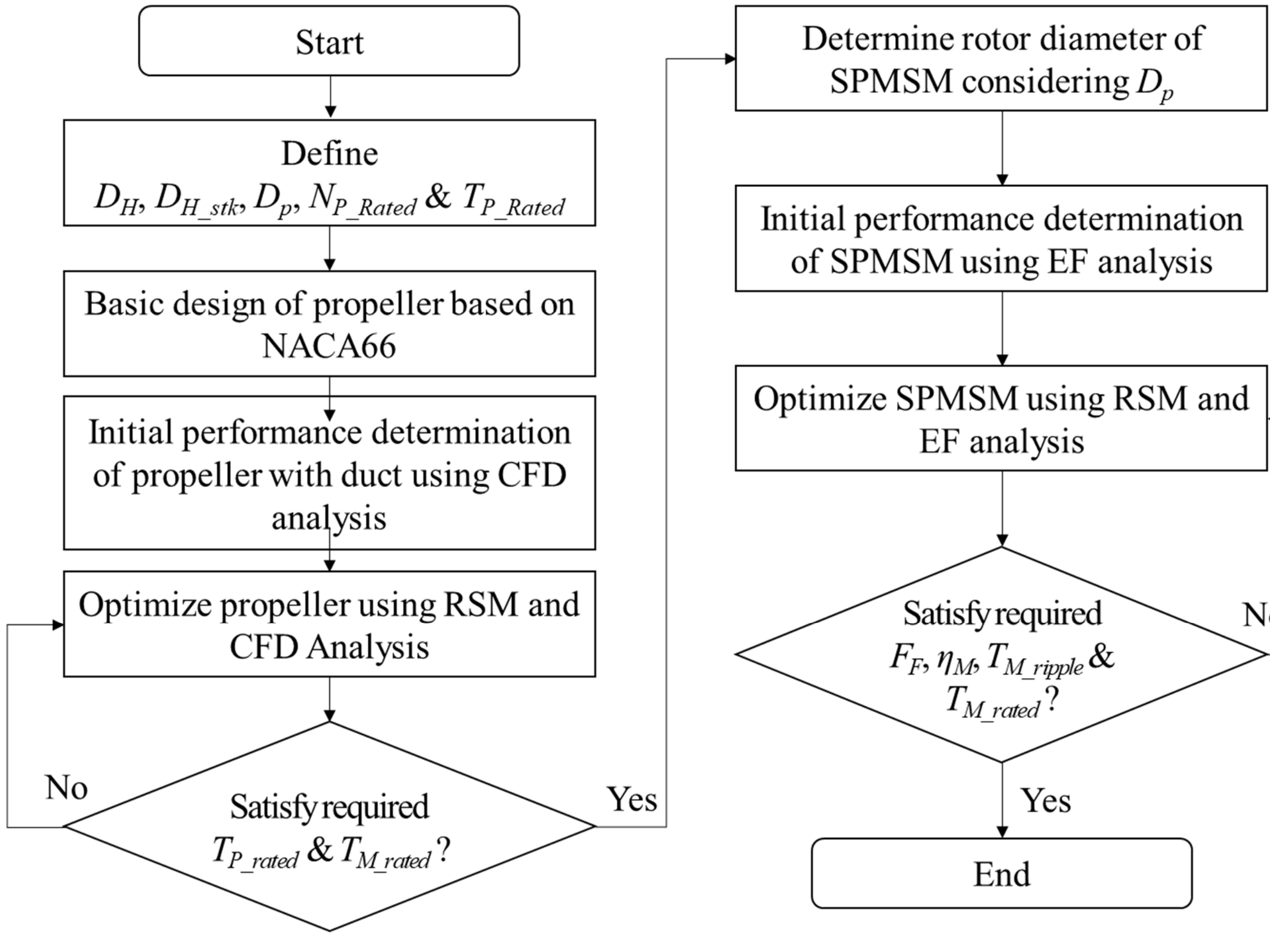

Figure 1. Flowchart for the design and analysis of HRDP.

Subsequently, for the optimization design of the propeller using the RSM, the thrust and torque of the propeller are defined as objective functions. The pitch (P), chord length (c), and camber (f) of the propeller are selected as factors that directly influence the objective function [34,35]. To standardize the factors, pitch was represented as the pitch diameter ratio (P/D_P), chord length was expressed as the chord length ratio (c/D_P), and camber ratio (f/c) was defined as the ratio between blade camber and chord length ratio.

For the 3D shape design of the hubless propeller, the airfoil of the blade was based on the NACA66 profile. The simplicity and standardization of the NACA66 profile facilitates the ease of design and manufacturing, further contributing to its widespread adoption in ship propeller applications [36].

To represent changes in the chord length ratio (c) of the propeller based on each radius ratio, the following equation can be used:

$$c = \alpha\left(1 - e^{-\frac{r_R}{\beta}}\right) \quad (1)$$

where r is the radial distance from the center hub of the propeller, R is the total radius of the propeller, r_R is the non-dimensional radius ratio, and α and β are the coefficients used to vary the r_R.

Table 3 shows the initial design values for the propeller. The CFD analysis was performed using the flow simulation tool in SolidWorks 2016. Figure 2 shows how the boundary conditions for the CFD analysis were configured.

Table 3. Initial design values for the propeller.

Item	Value
Alpha (α)	0.6
Beta (β)	0.7
Pitch diameter ratio (P/D_P)	2.4
Camber ratio (f/c)	0.1

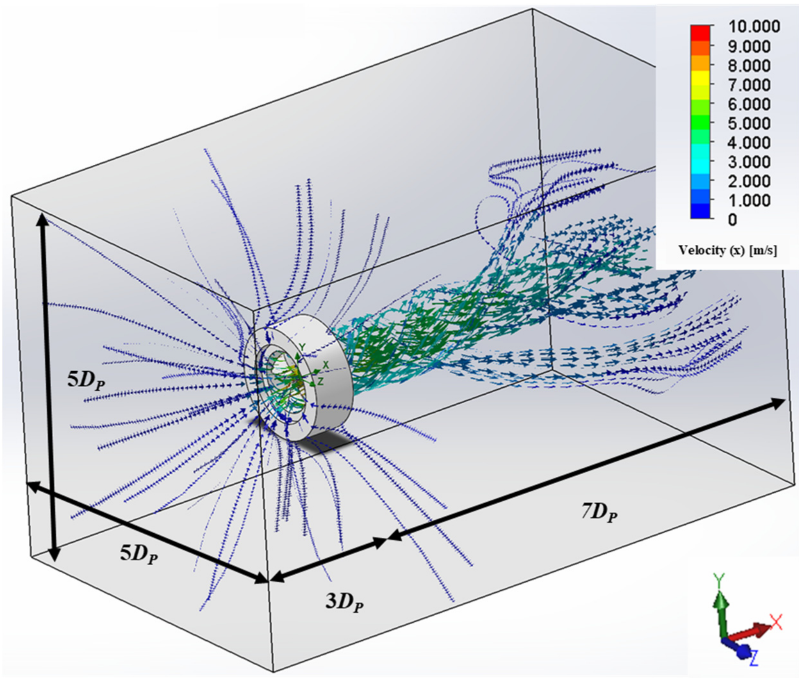

Figure 2. Boundary conditions for the CFD analysis.

The entire flow field is divided into two distinct regions: a rotating domain that encompasses the propeller, stator, and the inner surface of the duct, and a static domain comprised of other components. To establish the dimensions and locations of these various computational domains, a Cartesian coordinate system is employed. The origin, denoted as O, is centered at the blade's core, with the positive x-axis pointing in the direction of the free flow.

The inlet of the static domain, characterized by all sides spanning $5D_p$ in length, is situated $3D_p$ upstream of the HRDP. In contrast, the outlet is positioned $7D_p$ downstream from the HRDP. Within the computational domain, the fluid is modeled as water. At the inlet, the velocity is set to 0 m/s, establishing an advance ratio J of 0. The outlet is governed by a static pressure condition.

At the rated speed of 3300 rpm, the rated thrust of the initial propeller is 28.6689 N, and the required torque is 0.373902 Nm. This exceeds the rated thrust in the required specifications by approximately 3 N. A higher rated torque would result in an increased output rating for the SPMSM, consequently increasing the volume of the SPMSM. Therefore, it is necessary to satisfy the rated thrust of 25 N while minimizing the rated torque.

The MINITAB 16, a software package for statistical analysis and data analysis, was used for the RSM analysis. The range for α is set between 0.4 and 0.7, the range for β is between 0.5 and 0.8, the range for P/D_P is set between 1.4 and 2.6, and the range for f/c is set between 0 and 0.15. Figure 3 represents an optimization plot of the propeller using the RSM. The optimized factors have been selected as follows: α is 0.55, β is 0.65, P/D_P is 1.9974, and f/c is 0.2250. The confidence level is 97.677%. The RSM results reveal the following values: the thrust is 25.325 N and the required torque is 0.3 Nm. It can be confirmed that all the specifications have been met.

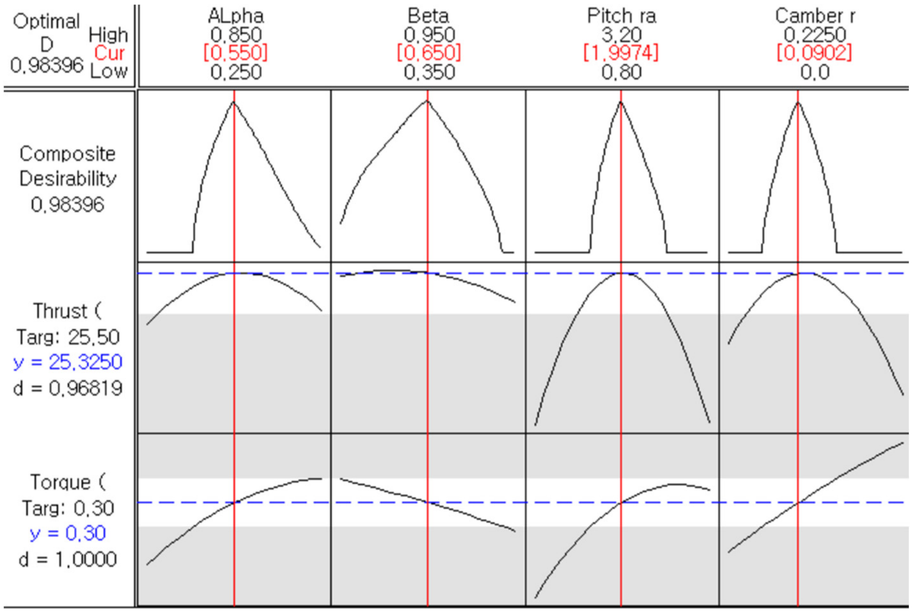

Figure 3. Optimization plot of propeller.

Figure 4a–c illustrate the cross-sections of the initial blade and the optimized blade on the XY plane as a function of the radius ratio R of the propeller. Figure 4d shows the 3D shape of the optimized propeller. The CFD analysis for the optimized propeller was conducted using the same boundary conditions as those of the initial propeller in Figure 2.

Compared to the initial propeller, the optimized propeller exhibits a rated thrust of 25.7295 N, which is approximately a 2.93 N reduction, and a rated torque of 0.302528 Nm, which also decreased by about 0.071% as Table 4 shows. The optimized propeller, with thrust values close to the target of 25 N and reduced required torque, enables energy savings at the rated speed of 3300 rpm by reducing power consumption to approximately 24.66 W.

Table 4. Performance comparison between the initial propeller and optimized propeller.

Item	Unit	Initial	Optimized
Rated thrust of HRDP (T_{P_rated})	N	28.6689	25.7295
Required torque of HRDP (Q_{P_rated})	Nm	0.373902	0.302528

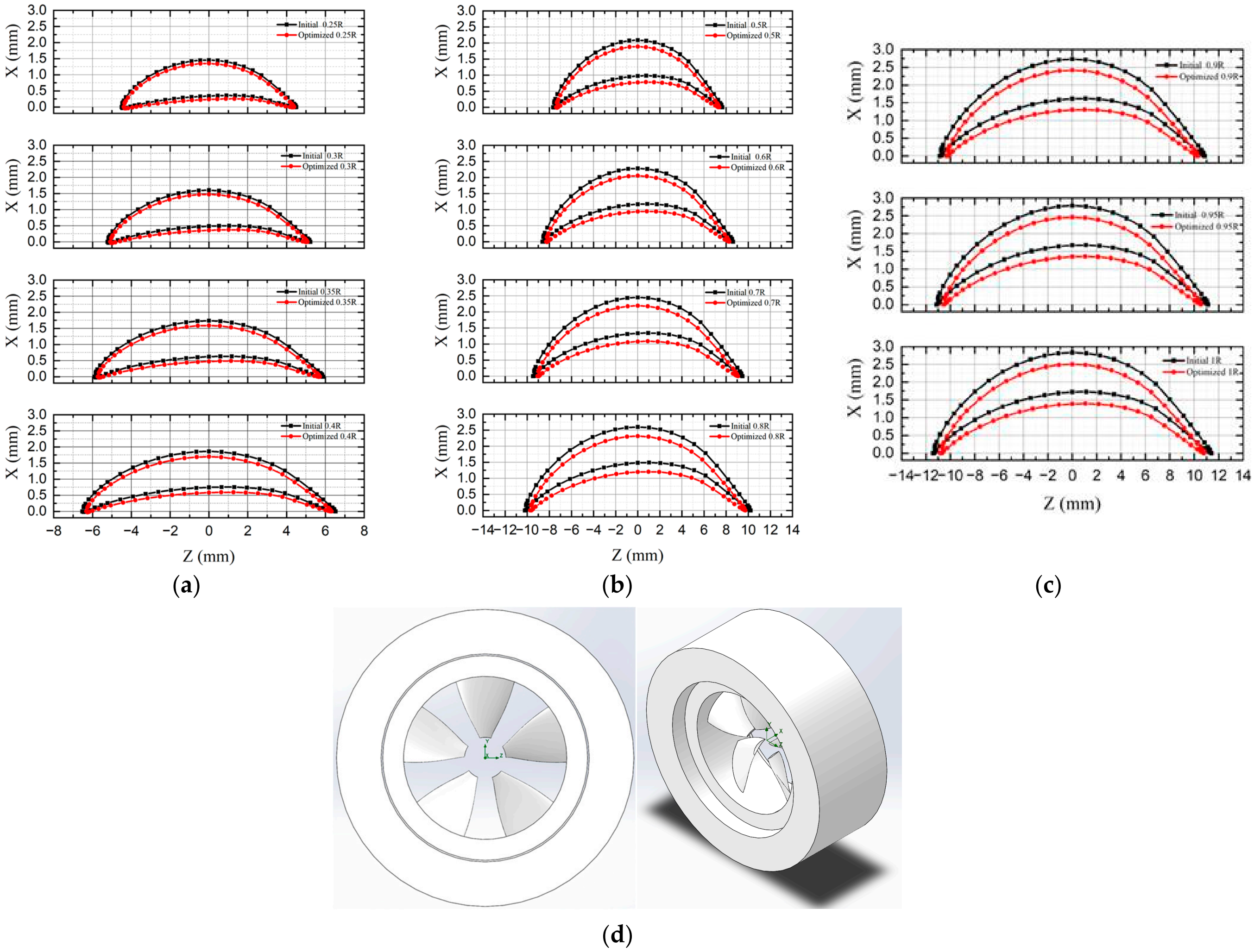

Figure 4. Shape comparison between initial propeller and optimized propeller: (**a**) Blade cross-sections from 0.25 R to 0.4 R; (**b**) Blade cross-sections from 0.5 R to 0.8 R; (**c**) Blade cross-sections from 0.9 R to 1 R; (**d**) Optimized propeller.

Figure 5 illustrates the performance comparison of the thrust and required torque between the initial propeller and optimized propeller according to the speed using CFD analysis. Compared to the initial propeller, it can be confirmed that the thrust of the optimized propeller decreased across all speed ranges, leading to a corresponding reduction in torque. The torque-thrust ratio *TTR* can be expressed as follows:

$$TTR = \frac{Q_P}{T_P} \tag{2}$$

where Q_P is the required torque of the propeller and T_P is the thrust of the propeller. A higher value of *TTR* indicates a greater required torque to generate any given thrust. In all operating speed ranges in Figure 5d, the *TTR* value of the optimized propeller was reduced to 0.0116~0.0122, compared to the *TTR* value of the initial propeller, which ranged from 0.013 to 0.1887. This result is possible to save energy because the required torque is minimized while meeting the required thrust specifications.

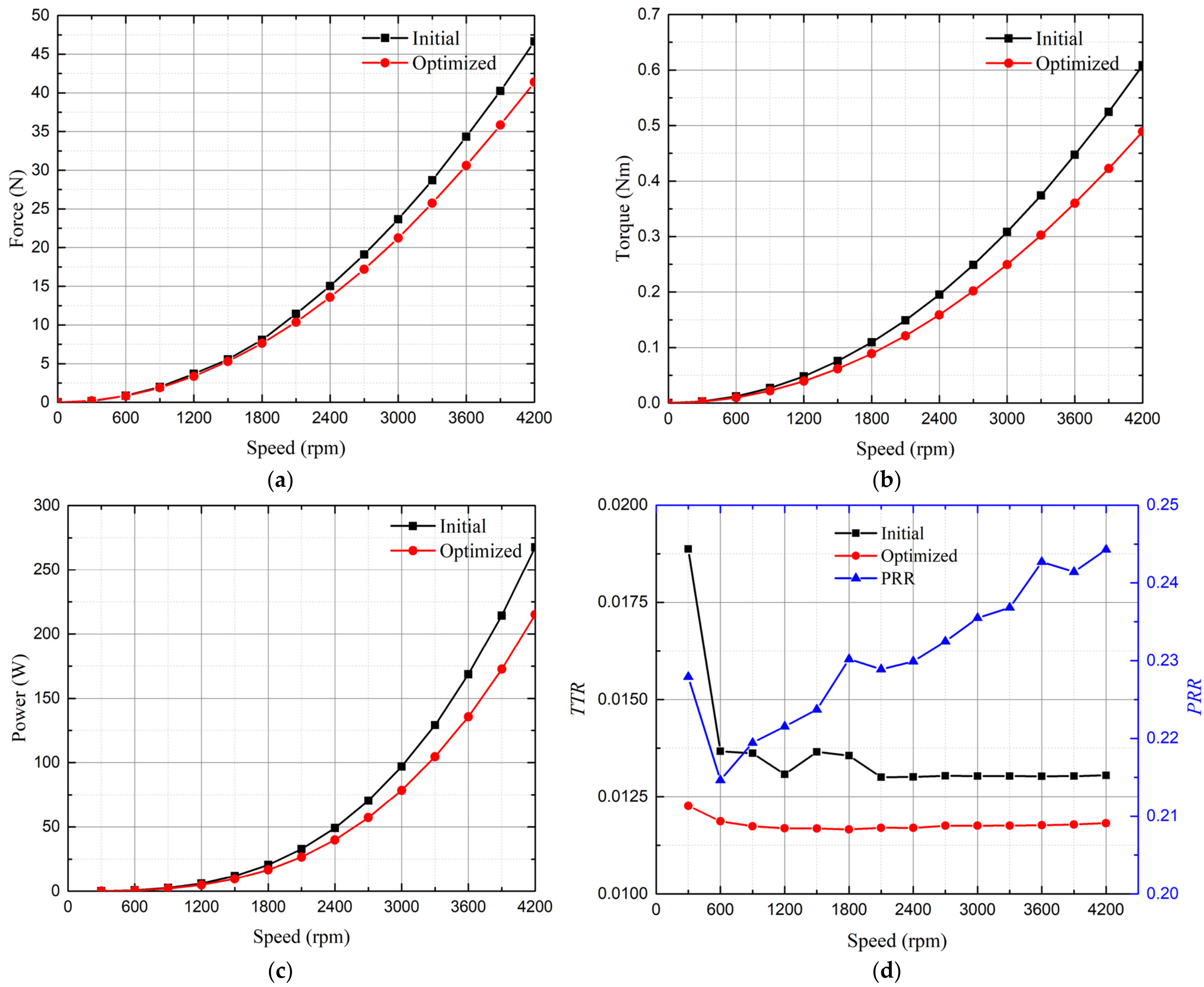

Figure 5. Performance comparison between initial propeller and optimized propeller according to speed using CFD analysis: (**a**) Thrust; (**b**) Required torque; (**c**) Mechanical power; (**d**) *TTR* and *PRR*.

Figure 5c shows the mechanical output power of the propeller according to the speed. The mechanical output power of the propeller P_P can be expressed as follows:

$$P_P = \frac{2\pi}{60} N_P \tag{3}$$

where N_P is the speed of the propeller. The reduction ratio *PRR* in Figure 5d can be expressed as follows:

$$PRR = \frac{P_{Initial} - P_{Optimized}}{P_{Optimized}} \tag{4}$$

where $P_{initial}$ is the mechanical output power of the initial propeller and $P_{optimized}$ is the mechanical output power of the optimized propeller. In Figure 5d, the *PRR* values are all positive, ranging from 0.2146 to 0.2442, which means that power consumption is reduced, so replacing the initial propeller with an optimized propeller can increase the operating time of the unmanned underwater drone.

2.3. Design and Analysis of SPMSM

According to the results in Table 3, the required torque for achieving a rated thrust of 25.7295 N with the optimized propeller should be greater than or equal to 0.3 Nm. Table 5 represents the required specifications of the SPMSM to drive the optimized propeller. The objective functions chosen for the use of the RSM are as follows: the winding fill factor of 0.35 or less for ease of manufacturing, efficiency of 90% or higher for power consumption minimization, a torque ripple affecting noise and vibration of 3% or less, and an output torque of at least 0.3 Nm.

Table 5. Required specifications of SPMSM.

Item	Unit	Value
Winding fill factor (F_F)	-	$\leq$0.35
Efficiency (η_M)	%	$\geq$90
Torque ripple (T_{M_ripple})	%	$\leq$3
Output torque (T_{M_rated})	Nm	$\geq$0.3

When satisfying the rated thrust at the rated speed of the propeller, the selection of the rotor diameter of the SPMSM is based on the propeller diameter in Figure 1. The diameter of the propeller (D_P) is 52 mm, so the inner diameter of the rotor core was chosen as 54 mm, taking into account a 1 mm epoxy injection space for the coupling between the propeller and the rotor core. To prevent water ingress in underwater conditions, it is necessary to apply epoxy coating to both the rotor and stator. Therefore, a 2 mm airgap length was sufficiently chosen to prevent mechanical interference between the rotor and stator.

The torque per unit of the rotor volume (TRV) for selecting the rotor size of the SPMSM can be expressed as follows [37]:

$$TRV = \frac{\pi}{\sqrt{2}} k_{w1} AB \tag{5}$$

where k_{w1} is the fundamental harmonic winding factor, A is the electric loading, and B is the magnetic loading. The electric field and magnetic field can be expressed as follows:

$$A = \frac{2mT_{ph}I}{\pi D} \tag{6}$$

$$B = \phi_1 \frac{2p}{\pi D L_{stk}} \tag{7}$$

where m is the number of phases, T_{ph} is the number of turns in series per phase, I is the RMS phase current, D is the diameter of the airgap, ϕ_1 is the flux density, p is the number of pole pair, and L_{stk} is the stack length.

The HRDP is used in an unmanned underwater drone powered by DC 16 V, and the SPMSM is supplied with the electrical power through an inverter capable of vector control based on the speed PI controller and current PI controller [38]. Therefore, it is necessary to determine the back electromotive force (BEMF) based on the upper voltage limit of the SPMSM and select the rated current accordingly.

Table 6 represents the results of the basic design of the SPMSM using Equations (5)–(7). Figure 6a represents the initial shape of the SPMSM based on the basic design.

Figure 7 and Table 7 present the performance comparison of the initial SPMSM and the optimized SPMSM. The initial SPMSM satisfies the required specifications with 91.33% at a rated current of 10.5 A and an output torque of 0.31995 Nm. However, the winding fill factor is 0.3926 and the torque ripple is 3.4647%, which does not satisfy the required specifications in Table 4, so it is necessary to satisfy them through optimization design.

Table 6. Basic design results of SPMSM using *TRV*.

Item	Unit	Value
Number of poles/slots		10/12
RMS phase current (I)	A	10.5
Number of phases	-	3
Number of turns in series per phase (T_{ph})	-	32
Electric loading (A)	A/m	9872.5
Magnetic lading (B)	T	0.314
Line to lien BEMF (E)	V_{rms}	6.08
Stack length (L_{stk})	mm	15
Current density (J)	A/mm^2	5.072
Torque per unit of rotor volume (TRV)	kNm/m^3	6.43

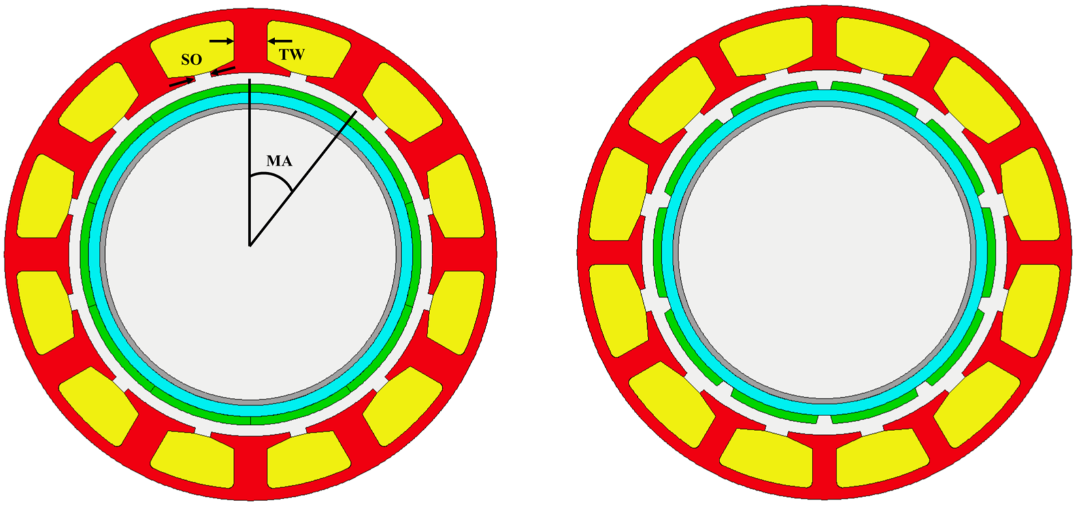

(**a**) (**b**)

Figure 6. Shape comparison between initial SPMSM and optimized SPMSM: (**a**) Initial SPMSM; (**b**) Optimized SPMSM.

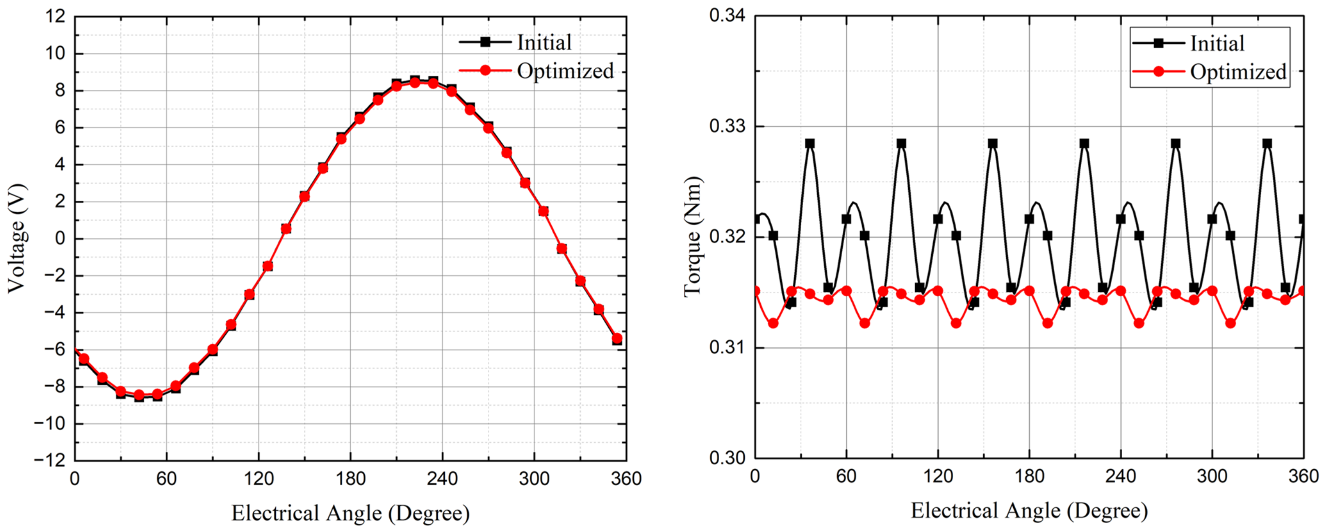

(**a**) (**b**)

Figure 7. Performance comparison between initial SPMSM and optimized SPMSM using EF analysis: (**a**) Line to line BEMF; (**b**) Output torque.

Table 7. Performance comparison between initial SPMSM and optimized SPMSM.

Item	Unit	Initial	Optimized
Winding fill factor (F_F)	-	0.3926	0.3493
Efficiency (η_M)	%	91.33	91.186
Torque ripple (T_{M_ripple})	%	3.4647	2.9789
Output torque (T_{M_rated})	Nm	0.31995	0.3143

To solve these problems, the optimization design of the SPMSM was performed using the RSM according to the procedure in Figure 1. The tooth width (TW), slot opening (SO), and magnet arc (MA) of the initial SPMSM are selected as factors that directly influence the objective function in Figure 6a. Figure 8 represents an optimization plot of the SPMSM using the RSM. The selected factor values are as follows: TW is 4.3437 mm, SO is 4.1204 mm, and MA is 151.1713 degrees, with a confidence level of 97.677%. The fill factor is 0.348, efficiency is 90.3767%, torque ripple is 2.99%, and the output torque is 0.3004 Nm. It can be confirmed that all the specifications have been met.

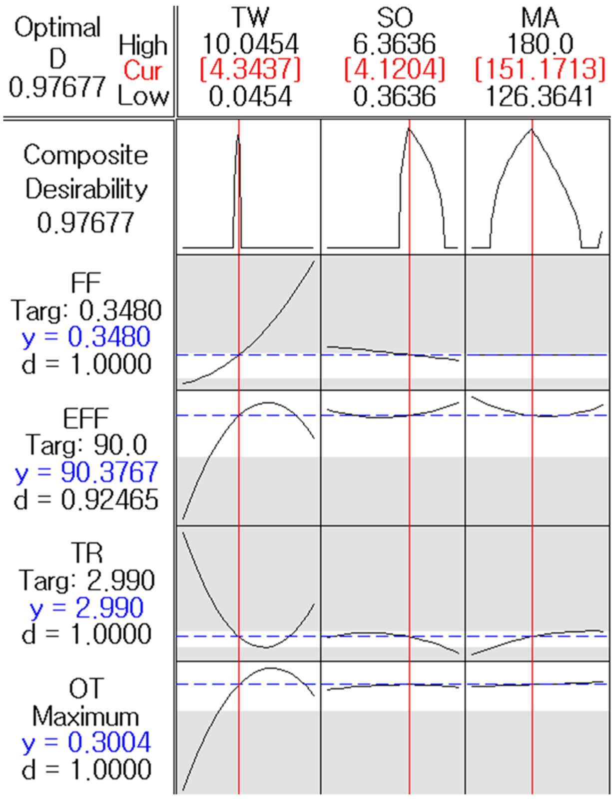

Figure 8. Optimization plot of SPMSM.

To validate the reliability of the RSM results, the selected factors were applied to create the shape in Figure 6b, followed by performing EF analysis. Compared to the initial SPMSM, the optimized SPMSM demonstrates an efficiency of 91.186%, with a slight reduction in output torque to 0.3143 Nm, which still satisfies the required specifications. Furthermore, the winding fill factor is 0.3493, and the torque ripple is 2.9789%, both of which also conform to the required specifications.

3. Experimental Results

3.1. Performance Test of HRDP

Figure 9a,b show the hubless propeller with the rotor of the SPMSM and the duct with the stator of the SPMSM. The initial weight of the active part of the SPMSM was 0.3805 kg, and after optimization, the weight of the SPMSM was reduced by about 7.3% to 0.3526 kg because the values of TW and MA decreased. Epoxy was injected to prevent water ingress in the duct made of the ABS, where the stator was inserted for underwater operation.

(a) (b)

Figure 9. Manufactured HRDP: (**a**) Hubless propeller with the rotor; (**b**) Duct with the stator.

Figure 10 illustrates the water tank test setup for the HRDP. The water tank was manufactured to match the dimensions used in the CFD analysis boundary conditions and the HRDP was installed in the same location as in Figure 5. DC 16 V was supplied to the controller from a DC power supply, and the controller drove the HRDP using the sensorless vector control. Power measurements were performed by connecting voltage probes and current probes to the input and output terminals of the controller. In the case of thrust, the load cell was connected to the guideline installed at the top of the water tank to enable measurement. The speed of HRDP was replaced with the value estimated by the controller. The measured values were all transmitted to the power analyzer, where electrical power and mechanical power were calculated.

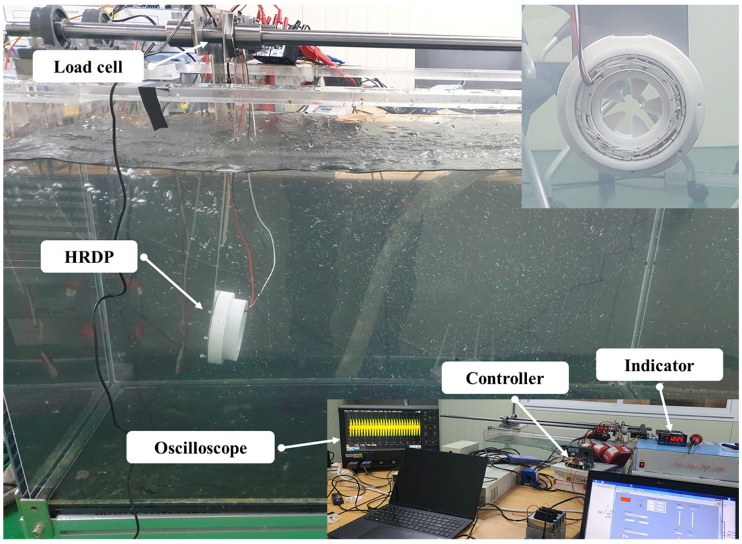

Figure 10. Water tank test setup of the HRDP.

Figure 11a represents the terminal line to line voltage and phase current of the HRDP at the rated speed of 3300 rpm. The rated thrust is 25.533 N, and the phase current is 10.33 A. The discrepancy with the EF analysis phase current of 10.5 A is due to variations in the BEMF value based on the temperature of the SPMSM and changes in thrust caused by flow fluctuations in the water tank.

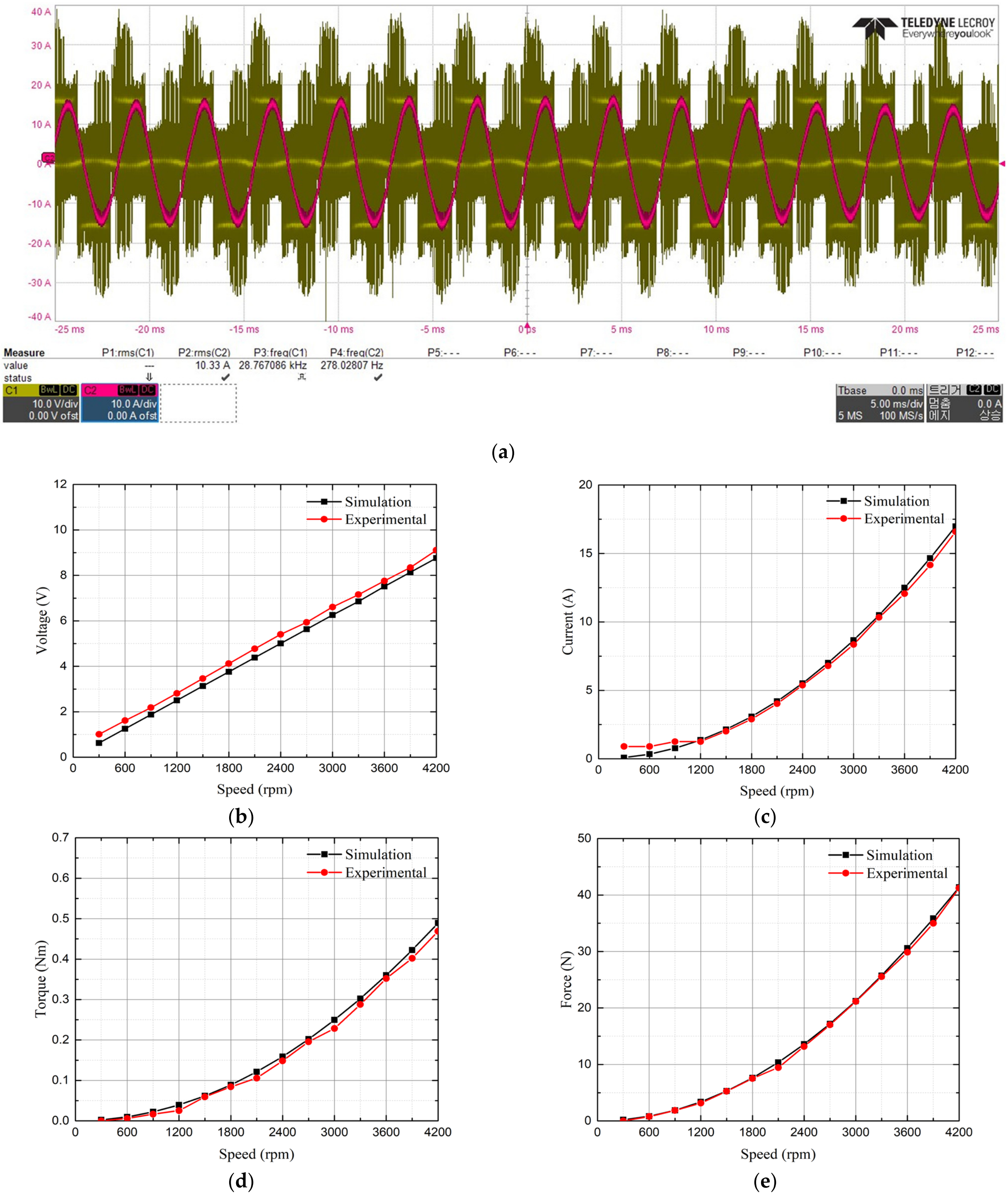

Figure 11. Comparison of simulation and experimental results: (**a**) Terminal line to line voltage and phase current of HRDP at rated speed of 3300 rpm; (**b**) Terminal line to line voltage according to speed; (**c**) Phase current according to speed; (**d**) Torque estimated from controller according to speed; (**e**) Thrust according to speed.

Figure 11b–e show a comparison between simulation results using CFD and EF analysis and experimental results. Compared with the simulation results, the experimental results show a higher terminal line to line voltage due to the increase in BEMF due to the temperature of SPMSM. As a result, the phase current decreased and the estimated torque value was also calculated low. However, in the case of thrust, the results that satisfy the required specifications can be confirmed.

3.2. Durability Test of HRDP

Table 8 shows command profiles with various speeds. There are a total of 8 sections, and except for section 5, which is 1.67 h, the HRDP runs continuously for 5 h in the remaining sections. The input pulse duty was defined for each section at the digital input port of the controller to change the speed of the HRDP.

Table 8. Command profiles with various speeds.

Section	Time (h)	Input Pulse Duty	Speed
1	5	50	1833
2	5	60	2200
3	5	70	2566
4	5	80	2933
5	1.67	90	3300
6	5	80	2933
7	5	70	2566
8	5	60	2200

Figure 12 shows the durability test results of the HRDP. The command profiles with various speeds were repeated a total of 20 times and operated continuously. Durability was verified by operating for a total of 733 h. It can be confirmed that the terminal line to line voltage of the controller is stably output as the feedback speed according to the command speed is stably driven. In the case of thrust, a slight ripple occurs due to a change in the flow rate of the water tank, so the phase current also generates a ripple. After completing the durability test, it was confirmed that there was no damage due to friction between the outer diameter of the rotor and the inner diameter of the stator.

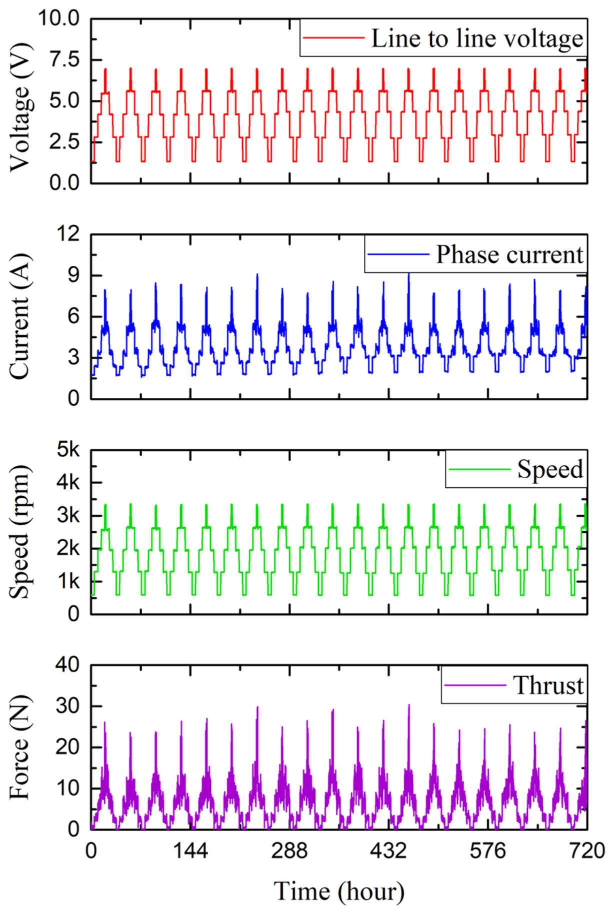

Figure 12. Durability test results of HRDP.

4. Conclusions

This paper presented a comprehensive study on the design and experimental validation of a HRDP intended for deployment in an unmanned underwater drone. The primary objective of this research was to reduce the dependence on traditional bearings and tackle the challenges associated with weight in battery-powered underwater systems. The study followed a systematic and structured approach, encompassing the optimization of both the propeller and the SPMSM within the HRDP system.

Regarding the HRDP, the initial design underwent a significant enhancement process, incorporating a combination of CFD analysis and the RSM. The results of this optimization effort revealed a HRDP with improved energy efficiency and reduced torque demands, leading to significant energy savings during underwater operation. The optimization of the SPMSM ensured that it met the specific requirements set out in the study, including winding fill factor, efficiency, torque ripple, and output torque.

The experimental results provided a robust confirmation of the HRDP's performance and durability, validating its capability to operate effectively under a range of speeds and environmental conditions. The alignment of the HRDP's performance with the specified requirements established its suitability for underwater drone applications.

In conclusion, the combined optimization efforts applied to both the HRDP and the SPMSM have yielded a more efficient and reliable propulsion system tailored for underwater drones. This approach not only fulfills environmental and energy efficiency goals but also holds significant promise for enhancing the capabilities of underwater robotic systems.

Author Contributions: Conceptualization, S.-A.K.; methodology, S.-A.K.; software, M.-S.K.; validation, S.-A.K.; formal analysis, M.-S.K.; investigation, M.-S.K.; writing—original draft preparation, M.-S.K.; writing—review and editing, S.-A.K.; visualization, S.-A.K. All authors have read and agreed to the published version of the manuscript.

Funding: This work was partly supported by the Collabo R&D Program of MSS (S3301642) and the Full Cycle Technology Development of MOTIE (RS-2023-00255506).

Data Availability Statement: Not applicable.

Conflicts of Interest: The authors declare no conflict of interest.

References

1. Guk, J.; Park, D.; Kim, S.; Lim, H.; Jung, S.P. Current Status and Perspectives of Eco-friendly Electric Ships. *J. Korean Soc. Environ. Eng.* **2023**, *45*, 256–266. [CrossRef]
2. Shim, H.; Kim, Y.H.; Hong, J.-P.; Hwang, D.; Kang, H.J. Marine Demonstration of Alternative Fuels on the Basis of Propulsion Load Sharing for Sustainable Ship Design. *J. Mar. Sci. Eng.* **2023**, *11*, 567. [CrossRef]
3. Kim, S.-A. A Study on the Predictive Maintenance Algorithms Considering Load Characteristics of PMSMs to Drive EGR Blowers for Smart Ships. *Energies* **2021**, *14*, 5744. [CrossRef]
4. Sung-An, K. Remaining life prediction algorithms of electric motors for exhaust gas recirculation blower systems. *J. Adv. Mar. Eng. Technol.* **2022**, *46*, 6. [CrossRef]
5. Reusser, C.A.; Pérez Osses, J.R. Challenges for Zero-Emissions Ship. *J. Mar. Sci. Eng.* **2021**, *9*, 1042. [CrossRef]
6. Shell. Greenhouse Gas Emissions in Shipping. Available online: www.shell.com/energy-and-innovation.html (accessed on 28 August 2021).
7. Lin, J.; Yao, H.D.; Wang, C.; Su, Y.; Yang, C. Hydrodynamic Performance of a Rim-Driven Thruster Improved with Gap Geometry Adjustment. *Eng. Appl. Comput. Fluid Mech.* **2023**, *17*, 2183902. [CrossRef]
8. Lin, J.; Han, Y.; Guo, C.; Su, Y.; Zhong, R. Intelligent Ship Anti-Rolling Control System Based on a Deep Deterministic Policy Gradient Algorithm and the Magnus Effect. *Phys. Fluids* **2022**, *34*, 057102. [CrossRef]
9. Su, Y.; Lin, J.; Zhao, D.; Guo, C.; Wang, C.; Guo, H. Real-Time Prediction of Large-Scale Ship Model Vertical Acceleration based on Recurrent Neural Network. *J. Mar. Sci. Eng.* **2022**, *8*, 777. [CrossRef]
10. Grűmmer, H. Design and Optimization of a Hubless Rim-Driven Thruster for an Autonomous Surface Vehicle Using RANSE Simulation. Ph.D. Thesis, Department of Dynamics of Maritime Systems, Technical University of Berlin, Berlin, Germany, 2016.
11. Zhu, Z.; Liu, H. The external characteristics and inner flow research of rim-driven thruster. *Adv. Mech. Eng.* **2022**, *14*, 1–10. [CrossRef]

12. Freeman, M.D.; Marshall, M.A. An analytical investigation into the design of a shaftless thruster using finite element and computational fluid dynamics approaches. *J. Ocean Technol.* **2011**, *6*, 55–68. Available online: http://research.library.mun.ca/id/eprint/232 (accessed on 1 November 2023).
13. Chen, Y.; Wang, L.; Hua, H.X. Longitudinal vibration and unsteady thrust transmission of the rim driven thruster induced by ingested turbulence. *Ocean Eng.* **2017**, *131*, 149–161. [CrossRef]
14. Jiang, H.; Ouyang, W.; Sheng, C.; Lan, J.; Bucknall, R. Numerical investigation on hydrodynamic performance of a novel shaftless rim-driven counter-rotating thruster considering gap fluid. *Appl. Ocean Res.* **2022**, *118*, 102967. [CrossRef]
15. Yang, J.; He, W.; Li, Z. On Scale Effect of Rim-Driven Thruster Based on RANS Method. In Proceedings of the 30th International Ocean and Polar Engineering Conference, Virtual, 11–16 October 2020; OnePetro: Richardson, TX, USA, 2020.
16. Hieke, M.; Sultani, H.; Witte, M.; von Estorff, O.; Wurm, F.H. A workflow for hydroacoustic source analyses based on a scale-resolving flow simulation of a hubless propeller. *Ocean Eng.* **2022**, *261*, 112131. [CrossRef]
17. Zhang, S.; Zhu, X.; Zhou, Z.L. Hydrodynamic performance analysis of hubless rim-driven propulsors. *Appl. Mech. Mater.* **2013**, *256*, 2565–2568. [CrossRef]
18. Cao, Q.M.; Hong, F.W.; Tang, D.H.; Hu, F.L.; Lu, L.Z. Prediction of loading distribution and hydrodynamic measurements for propeller blades in a rim driven thruster. *J. Hydrodyn.* **2012**, *24*, 50–57. [CrossRef]
19. Gaggero, S. Numerical Design of a RIM-Driven Thruster using a RANS-based Optimization Approach. *Appl. Ocean Res.* **2020**, *94*, 101941. [CrossRef]
20. Liu, B.; Vanierschot, M.; Buysschaert, F. Effects of transition turbulence modeling on the hydrodynamic performance prediction of a rim-driven thruster under different duct designs. *Ocean Eng.* **2022**, *256*, 111142. [CrossRef]
21. Song, B.; Wang, Y.; Tian, W. Open water performance comparison between hub-type and hubless rim driven thrusters based on CFD method. *Ocean Eng.* **2015**, *103*, 55–63. [CrossRef]
22. Cai, M.; Yang, C.; Wu, S.; Zhu, Y.; Xie, Y. Hydrodynamic analysis of a rim-driven thruster based on RANS method. In Proceedings of the OCEANS 2015-MTS/IEEE Washington Conference, Washington, DC, USA, 19–22 October 2015; IEEE: New York, NY, USA, 2015; pp. 1–5. [CrossRef]
23. Cao, Q.M.; Zhao, W.F.; Tang, D.H.; Hong, F.W. Effect of gap flow on the torque for blades in a rim driven thruster without axial pressure gradient. *Procedia Eng.* **2015**, *126*, 680–685. [CrossRef]
24. Moukalled, F.; Mangani, L.; Darwish, M. *The Finite Volume Method in Computational Fluid Dynamics*; Springer: Berlin/Heidelberg, Germany, 2016; Volume 113. [CrossRef]
25. Dubas, A.J.; Bressloff, N.W.; Sharkh, S.M. Numerical modelling of rotor–stator interaction in rim driven thrusters. *Ocean Eng.* **2015**, *106*, 281–288. [CrossRef]
26. Baltazar, J.; Falcão de Campos, J.A.C.; Bosschers, J. Open-water thrust and torque predictions of a ducted propeller system with a panel method. *Int. J. Rotating Mach.* **2012**, *2012*, 474785. [CrossRef]
27. Liu, B.; Vanierschot, M. Numerical Study of the Hydrodynamic Characteristics Comparison between a Ducted Propeller and a Rim-Driven Thruster. *Appl. Sci.* **2021**, *11*, 4919. [CrossRef]
28. Li, Y.; Song, B.; Mao, Z.; Tian, W. Analysis and Optimization of the Electromagnetic Performance of a Novel Stator Modular Ring Drive Thruster Motor. *Energies* **2018**, *11*, 1598. [CrossRef]
29. Gaggero, S. A Study on the Wake Evolution of a Set of RIM-Driven Thrusters. *J. Mar. Sci. Eng.* **2023**, *11*, 1659. [CrossRef]
30. Amri, L.; Zouggar, S.; Charpentier, J.-F.; Kebdani, M.; Senhaji, A.; Attar, A.; Bakir, F. Design and Optimization of Synchronous Motor Using PM Halbach Arrays for Rim-Driven Counter-Rotating Pump. *Energies* **2023**, *16*, 3070. [CrossRef]
31. Wang, B.; Ouyang, W.; Wang, S.; Sheng, C.; He, T.; Yan, Z. Load Carrying Capacity Enhancing Design and Lubrication Investigation of the Magnetic-Water Double Suspension Elastic Support Thrust Bearing. *Lubricants* **2023**, *11*, 401. [CrossRef]
32. Kim, S.A. A Study on the Optimal Design of Built-in Electric Motor for Driving Integrated Flywheel. *Trans. Korean Inst. Electr. Eng.* **2020**, *69*, 1349–1355. [CrossRef]
33. Kim, S.A.; Park, S.K.; Cho, Y.H. Design of brushless DC motor with weight reduction and performance improvements considering twelve step control. *Int. J. Appl. Electromagn. Mech.* **2019**, *59*, 729–736. [CrossRef]
34. Nie, Y.; Ouyang, W.; Zhang, Z.; Li, G.; Zheng, R. Multi-Parameter Optimization Analysis of Hydrodynamic Performance for Rim-Driven Thruster. *Energies* **2023**, *16*, 891. [CrossRef]
35. Liang, X.; Yan, X.; Ouyang, W.; Liu, Z. Experimental research on tribological and vibration performance of water-lubricated hydrodynamic thrust bearings used in marine shaft-less rim driven thrusters. *Wear* **2019**, *426*, 778–791. [CrossRef]
36. Srinivas Prasad, S.; Pardhasaradhi, N.; Durga Rao, K. Hydrodynamic Performance and Acoustic Response of Ship Propeller. *Trans. Marit. Sci.* **2023**, *12*, 1–10. [CrossRef]
37. Park, J.-H.; Lee, T.-W.; Jeong, Y.-H.; Hong, D.-K. Novel Multi-Physics Computational Simulation of a 10 kW Permanent Magnet Motor for Podded Propulsion. *Energies* **2022**, *15*, 6607. [CrossRef]
38. Bucolo, M.; Buscarino, A.; Fortuna, L.; Frasca, M. Forward Action to Stabilize Multiple Time-Delays MIMO Systems. *Int. J. Dyn. Control* **2023**, 1–9. [CrossRef]